Electronic Properties of Antimony Doped Anatase TiO2

Davinder S. Bhachu[1], Claire J. Carmalt[1], Russell G. Egdell[2] and Ivan P. Parkin[1*]

[1] Materials Chemistry Centre, Department of Chemistry, University College London
20 Gordon Street, London WC1H 0AJ, UK
[2] Department of Chemistry, University of Oxford, Inorganic Chemistry Laboratory,
South Parks road, Oxford OX1 3QR, UK

Abstract

The electronic properties of antimony doped anatase (TiO2) thin films deposited *via* aerosol assisted chemical vapour deposition were investigated by a range of spectroscopic techniques. The incorporation of Sb(V) into the TiO2 lattice was characterised by X-ray absorption spectroscopy and resulted in *n*-type conductivity, with a decrease in sheet resistance by four-orders of magnitude compared to that of undoped TiO2 films. The films with the best electrical properties displayed charge carrier concentrations of *ca.* 1×10^{20} cm^{-3} and a specific resistivity as low as 6×10^{-2} Ω.cm. Doping also resulted in orange colouration of the films that became progressively stronger with increasing Sb content. X-ray photoelectron spectroscopy showed that substantial segregation of Sb(III) to the surface of the film was associated with the appearance of "lone pair" surface states lying above the top of the main O 2p valence band. Pronounced visible region absorption in the films is attributed to transitions from Sb(III) states at surface and grain boundary interfaces into the conduction band. The segregation of Sb leads to p-type surface layers at high doping levels.

***Corresponding author
E-mail: i.p.parkin@ucl.ac.uk.
Fax: (+44) 20-7679-7463

1. Introduction

Titanium dioxide (TiO_2) is an abundant and non-toxic material that has long been recognized for its photocatalytic activity. It has many environmental applications in areas such as water purification, air purification and waste treatment. TiO_2 has also been used for catalytic water-splitting and as anti-bacterial coatings or self-cleaning coatings on glass. There are yet further applications as photoanodes in dye sensitized solar cells (DSSCs) and in gas sensing devices.[1–7] More recently, interest has developed in the use of doped TiO_2 as an alternative to conventional transparent conducting oxides (TCOs) such as Sn-doped In_2O_3 aka indium tin oxide (ITO), F-doped SnO_2 (FTO) and Al-doped ZnO (AZO). This work is driven mainly by the relatively high and extremely volatile cost of the indium required for ITO, coupled with the inferior performance of the alternative established TCOs such as FTO and AZO in terms of electron mobility and sheet conductivity. The cost of indium was $500/kg in 2009 compared to only $0.53/kg for titanium. Historically the price of indium has been as high as $1000/kg.[8,9]

The two most important polymorphs of TiO_2 are anatase and rutile. Both adopt tetragonal structures, but the volume per formula unit is bigger for the anatase phase. The bandgap of anatase (3.20 eV) is slightly bigger than that of rutile (3.06 eV) and the gap is indirect for anatase, whereas rutile has a direct bandgap.[10,11] Oxygen vacancies in both phases can introduce n-type conductivity by generating excess electrons that can act as charge carriers, leading to reduced sheet resistance:

$$O_O^X \leftrightarrow V_O^{\cdot\cdot} + 1/2 O_{2(g)} + 2e' \tag{1}$$

However there is a tendency for the electrons to self-trap onto polaronic Ti(III) centres.[12] Thus one major drawback of introducing oxygen vacancies is the subsequent loss of transparency[13] due to intense intervalence charge transfer transitions between Ti(III) and Ti(IV): on the basis of high resolution electron energy loss spectroscopy (HREELS) the oscillator strength of these transitions has been estimated to be as high as 0.10.[14] An alternative approach to introducing n-type charge carriers is the substitution of lattice Ti(IV) with group 5 aliovalent dopant

atoms ions such as V, Nb or Ta. These all have an additional valence electron and and in principle should act as one electron donors if M(V) occupies a Ti(IV) site without introduction of further compensating defects. However in V-doped *rutile* TiO_2 the excess electrons are localised onto V(IV) sites and give a characteristic peak whose vertical ionisation energy is just over 2 eV below the conduction band minimum in photoemission spectroscopy.[15–17] Nb acts as a much shallower donor in rutile TiO_2 but electrons do not occupy the conduction band. Instead they self-trap onto Ti(III) sites, at least at low doping levels[18,19] and Nb-doped rutile prepared by solid state reaction between NbO_2 and TiO_2 assumes an intense blue colouration similar that in oxygen deficient rutile. It should also be noted that Nb-doped rutile is susceptible to compensation by cation vacancy acceptor states when prepared under moderate oxygen partial pressures[20]: Ta-doped rutile behaves similarly.[21] Thus single crystal Nb-doped rutile prepared by O-plasma assisted molecular beam epitaxy[22] transpires to be almost completely compensated, with zero occupation of d electron states.[18] The properties of the Nb-doped *anatase* polymorph of TiO_2 are completely different. Material prepared by pulsed laser deposition (PLD)[13,23] or atmospheric pressure chemical vapour deposition (APCVD)[24] is both optically transparent in the visible region and highly conducting. Nb-doped anatase (NTO) films with resistivites as low as 4.6×10^{-4} Ω.cm have been prepared on glass substrates using pulsed laser deposition (PLD), meeting the low resistivites ($\rho < \times 10^{-3}$ Ω.cm) required for practical use as a TCO.[25] The basis of the differences between the two phases is unclear at present. Computational studies have offered little insight to date: depending on the Hamiltonian employed in the calculations electrons have been predicted to be either delocalised[26] or localised[19,27] in the Nb-doped anatase phase as well as the rutile-doped phase[19]. Experimentally, photoemission studies of the Nb-doped anatase phase show the signatures of a system close to a metal to non-metal transition with a peak associated with delocalised coherent states close to the Fermi energy and a broader incoherent peak arising from localised states deeper in the gap.[28]

Antimony is an alternative potential n-type dopant. The ground state configuration of antimony is [Kr] $4d^{10}$ $5s^2$ $5p^3$. The bulk solid state chemistry of Sb is dominated by (III) and (V) oxidation states. Given the that the ionic radii of 6-coordinate Sb(V), Sb(III) and Ti(IV) are 0.60 Å, 0.76 Å and 0.61 Å, respectively, it is reasonable to assume that the substitutional doping of Ti (IV) with Sb(V) in TiO_2 could lead to the introduction of *n*-type conductivity. However Sb-doped *rutile* is a

white, non conducting material and there appears to be almost complete compensation of Sb(V) donors by cation vacancies[29,30] On the other hand calculations[27] suggest that the Sb donor level in Sb-doped *anatase* should lie at a similar energy to the Nb level. This naturally raises the question as to whether Sb-doped anatase exhibits TCO behaviour similar to the Nb-doped material. This paper reports the synthesis of Sb-doped anatase TiO_2 thin films by aerosol assisted chemical vapour deposition (AACVD). The films were found to be highly conducting. The electronic properties of the Sb doped TiO_2 films were probed using X-ray absorption spectroscopy (XAS) and valence and core level photoemission spectroscopy (PES). The results of the X-ray spectroscopic measurements are discussed in relation to the transport properties and optical spectra.

2. Experimental

2.1 Sample preparation

Aerosol assisted chemical vapour deposition (AACVD) was conducted using a horizontal bed cold wall reactor. Glass substrates were place on a graphite block containing a Whatman cartridge heater, controlled using a Pt-Rh thermocouple. $Sb(OEt)_3$ was added to $Ti(OEt)_4$ (2 g, 8.8 mmol) in dopant quantities (0 mol.%, 1 mol.%, 2.5 mol.%, 10 mol.% and 20 mol.%) and the mixture was dissolved in toluene (30 mL) and stirred. The resultant solutions were placed in a flat-bottomed Schlenk-flask and an aerosol of sub-micrometre droplets was generated using a piezoelectric transducer beneath the flask. A nitrogen carrier gas was passed through the flask at a flow of 0.8 Lmin^{-1}.[5,31] The glass substrates were kept at 500 °C during deposition, and were subsequently allowed to cool to below 100 °C under a flow of nitrogen once all of the precursor solution had been exhausted. All films were deposited on 145 x 45 x 3 mm SiO_2 coated float-glass substrates (NSG) to minimise the effects of ion diffusion from the soda-lime glass into the film. Substrates were cleaned using isopropyl alcohol and were subsequently dried using a stream of air.

2.2 Film characterisation

X-ray diffraction (XRD) was patterns were measured in a modified Bruker-Axs D8 diffractometer with parallel beam optics equipped with a PSD LynxEye silicon strip detector to collect diffracted X-ray photons. This instrument uses a Cu source for X-ray generation with $CuK\alpha_1$ and $CuK\alpha_2$ radiation of wavelengths 1.54056 Å and 1.54439 Å respectively, emitted with an intensity ratio of 2:1, a voltage of 40 kV and current of 40 mA. The incident beam angle was kept at 1° and the angular range of the patterns collected was $10° < 2\theta < 66°$ with a step size of 0.05° counted at 2 s/step. Scanning electron microscope (SEM) images and energy dispersive X-ray (EDX) spectra were obtained on a JSM-6301F Scanning Microscope Field Emission machine. Hall effect measurements were carried out using the van Der Pauw method to determine the sheet resistance, free carrier concentration (N) and mobility (μ). UV/Visible/near IR spectra were measured using a Perkin Elmer Fourier transform Lambda 950 UV/Vis spectrometer over a wavelength range of 300 nm to 2500 nm in the transmission mode. X-ray absorption spectroscopy at the Sb K edge were measured on the BM26A (DUBBLE) beamline on the European Synchrotron Radiation Facility (ESRF) in Grenoble France which operated at 6 GeV with typical currents of 100 mA. The beamline incorporates a double crystal Si(111) monochromator, ion chambers for measuring incident and transmitted beam intensities and a 9-element monolithic fluorescence detector. All Sb K edge data were collected in fluorescence mode and and typically 8 scans were averaged to improve signal to noise. Spectra were processed using ATHENA software[31] and subsequent analysis of extended X-ray absorption fine structure (EXAFS) was performed using XCURVE software[32]. Core and valence level X-ray photoelectron spectroscopy (XPS) was carried out using a Thermo Scientific K-Alpha instrument with a monochromatic Al-K_α source. Curve fits to the core level peaks were made using using CasaXPS software after calibration of binding energies using the C 1s peak of adventitious carbon, assumed to be at 284.50 eV.

3. Results and discussion

3.1 Film characteristics, phase analysis and morphology.

The depositions resulted in a series of conformal TiO_2 films with optical interference fringes indicating that the films were thickest in the middle of the substrate (see below for discussion of optical spectra). The undoped TiO_2 film was transparent and but developed a progressively more intense orange colouration with increasing antimony doping. Transparency was lost and opaque blackened films were deposited at or above 20 mol.% Sb doping. These were deemed unsuitable for use as a TCO and were not studied further. Above 2.5 mol.% Sb the films showed an increasing number of dark aggregates on the surface of the film. These aggregates appeared lustrous under the microscope and were indicative of elemental antimony, which was confirmed by XRD. This suggests that the incorporation of Sb in the TiO_2 lattice may be kinetically inhibited under these conditions, instead favouring the reduction of $Sb(OEt)_3$ to Sb. Previous solid state studies have shown bulk Sb solubilities of 5% and above are possible in rutile TiO_2.[29,32]

The XRD patterns for the deposited films are shown in Fig. 1. All of the deposited films were crystalline giving diffraction patterns corresponding to the anatase polymorph of TiO_2. The texture coefficient (TC) of the films was used to determine preferred orientation. Preferred orientation was observed in (121) and (123) planes up to a doping level of 2.5 mol.%. The (123) plane was suppressed at doping levels of 10 mol.% with preferred orientation occurring in the (121)/(101) planes. The diffraction pattern for the 20% doped film is given in Figure 1 to demonstrate the appearance of diffraction peaks for both anatase and elemental antimony.
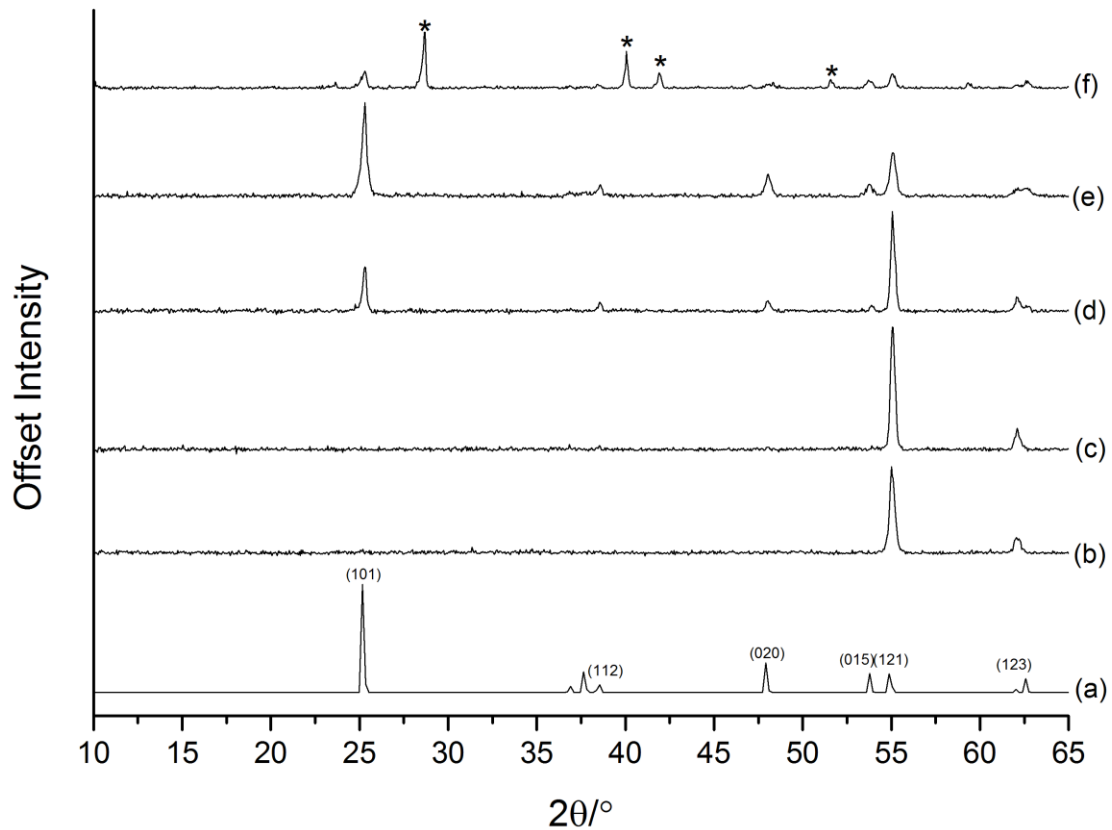
Figure 1: (a) Simulated XRD pattern for anatase TiO₂. (b) – (f) XRD patterns for the Sb-TiO₂ films deposited (b) 0 mol.% Sb, (c) 1 mol.% Sb, (d) 2.5 mol.% Sb, (e) 10 mol.% Sb and (f) 20 mol.% Sb. Peaks associated with elemental antimony are indicated with an asterisk (*).

The SEM images in Figure 2 show the variation in film microstructure with increasing Sb doping level. The size of the film features grow on initial doping to give pyramidal features at doping levels of 1 mol.% Sb. Increasing Sb doping levels in solution to 2.5 mol.% resulted in a change in the film microstructure Sb from pyramidal particle shapes to a mixture of pyramidal/needle-like features. Narrow and better-defined needle-like features become increasingly prominent with increased Sb doping. This needle-like microstructure is somewhat unusual for TiO₂ films as pyramidal particles are the most common for TiO₂ thin films. Film thicknesses were determined using cross-section SEM and are shown as insets within Figure 2 and listed in Table 1.
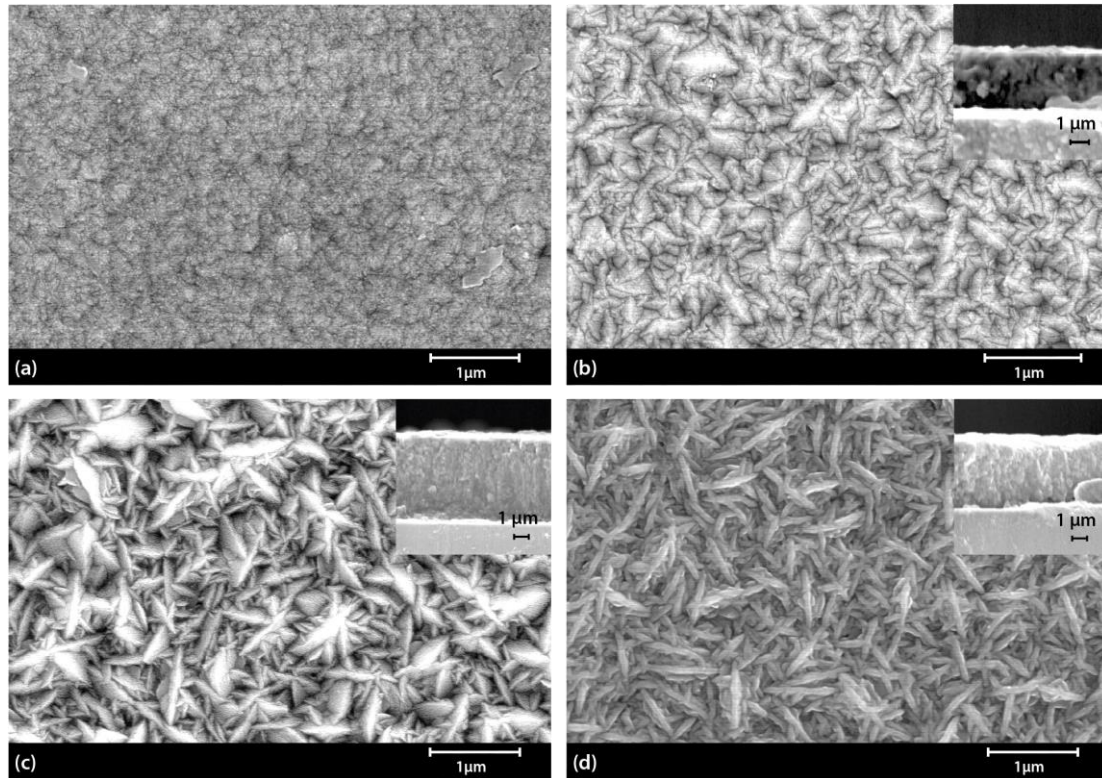
Figure 2 SEM images of the Sb:TiO$_2$ films deposited *via* **the AACVD decomposition of Ti(OEt)$_4$ with (a) 0 mol.% Sb, (b) 1 mol.% Sb (inset shows cross-section image), (c) 2.5 mol.% Sb (inset shows cross-section image) and (d) 10 mol.% Sb doping (inset shows cross-section image).**

3.2 Transport measurements and optical spectra.

The results of Hall effect measurements for the deposited films are shown in Table 1. Two-point probe measurements of the undoped TiO$_2$ showed too high a resistance (> 1 MΩ) for Hall effect measurements. At Sb doping levels of greater than 1 mol.% there is a decrease in the magnitude of the sheet resistance of the films compared to that of undoped TiO$_2$ by four orders of magnitude. Sb doping at a level of 2.5 mol.% resulted in the lowest sheet resistance of 130 Ω/sq. The sheet resistance subsequently increased when the Sb doping increased further to 10 mol.%. Hall effect measurements indicated that the films displayed *n*-type conductivity. Charge carrier concentration increased monotonically with Sb doping level as expected, whereas the mobility of the charge carriers decreased at the highest level of Sb doping after an initial increase with maximum mobility at 2.5 % doping. The carrier mobility is a function of carrier scattering time τ, which usually increases with scattering due to Coulombic interactions with ionised dopants amongst other species. The initial increase as the Sb doping level increases from 1% to 2.5% is therefore unusual.

Table 1: The dopant concentrations and electrical properties as determined by EDX and Hall effect measurements (respectively) of the AACVD deposited films .

Sb doping in solution /mol.%	[Sb]/ [Sb]+[Ti]$_{bulk}$	Film thickness / μm	Sheet resistance / Ω/sq	Resistivity ρ / Ωcm	Mobility / cm^2/Vs	Carrier concentration N /cm^3
0	0	2	-	-	-	-
1	0.011	3	93500	2.9×10^1	1.4×10^{-2}	-1.5×10^{19}
2.5	0.014	5	130	6.5×10^{-2}	8.2×10^{-1}	-1.2×10^{20}
10	0.036	4	211	9.7×10^{-2}	4.2×10^{-1}	-1.5×10^{20}

Optical spectra are shown in figure 4 in a Tauc plot of $(Ah\nu)^{1/2}$ versus photon energy $h\nu$ (here A is the absorption coefficient) as is appropriate for an oxide such as anatase with an indirect bandgap.[10,11]
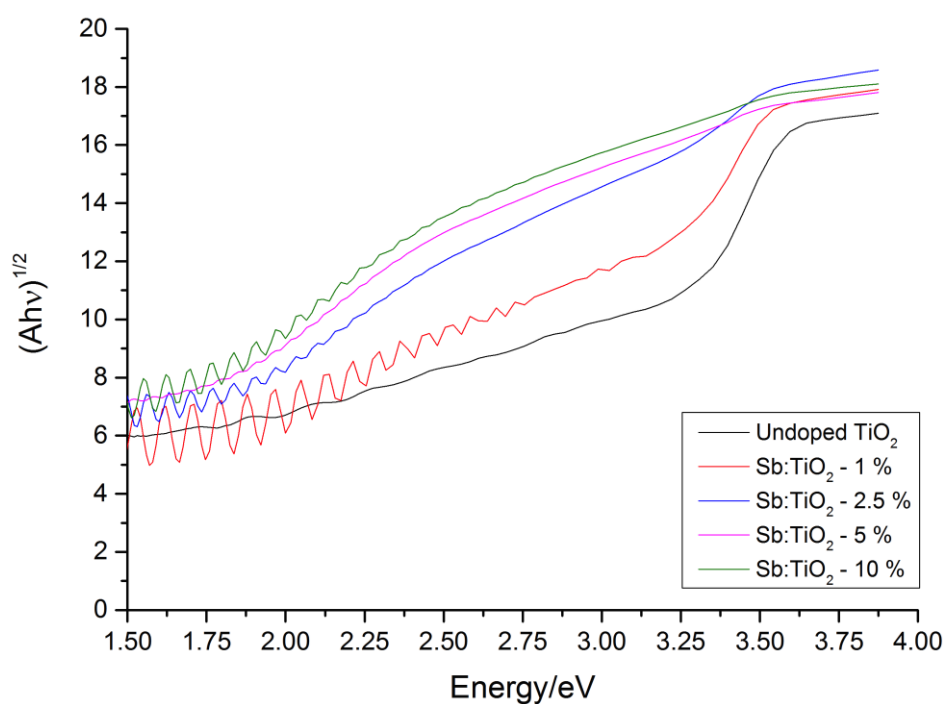

Figure 3: Optical absorption spectra of Sb-doped anatase as a function of doping level.

At low doping levels the main band edge at around 3 eV is well-defined and an optical bandgap value E_g for the films can be derived from linear extrapolation. The

value for anatase itself is close to 3.2 eV, in agreement with values reported elsewhere.[33] The band edge moves to lower energy with 1% Sb doping, but at the same time there is increased absorption across the visible region. For doping levels above 5% the main absorption edge merges completely with the visible region absorption and already by 2.5% doping the main edge is ill-defined. The red shift in the absorption edge is surprising given that a blue Moss-Burstein[34] shift might be anticipated due to conduction band filling. However in the closely related system where Sn is doped into TiO_2 bandgap narrowing is also observed.[35] The pronounced visible region absorption is also somewhat puzzling in that both the host TiO_2 and the oxides Sb_2O_3 and Sb_2O_5 are white solids.[36] We return to this topic after discussion of valence band photoemission structure in section 3.4. However here it should be noted that a declining absorption in moving from the blue through to the red region of the electromagnetic spectrum in itself accounts empirically for the pronounced yellow-brown colouration of the Sb-doped films.

3.2 X-ray absorption spectroscopy

K shell X-ray absorption spectra for 5% and 10% Sb-doped TiO_2 are shown in figure 5 along with reference spectra for Sb_2O_3 and Sb_2O_5. The absoption peaks for the doped samples were quite weak and the signal to noise in the spectra for samples with the two lower doping levels was rather poor so these spectra are not reproduced here.
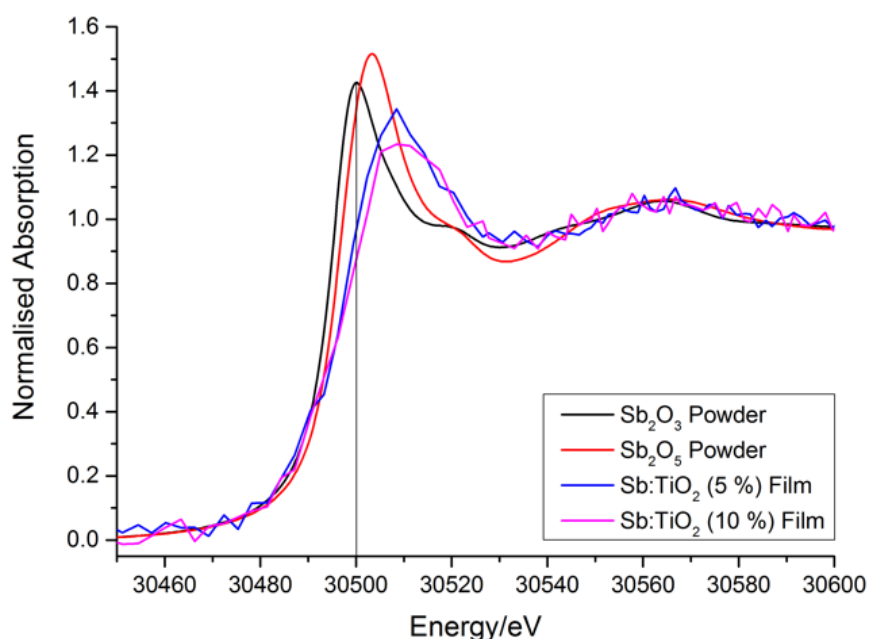
Figure 4: K shell X-ray absorption spectra 5% and 10% Sb-doped TiO₂ along with reference spectra for Sb₂O₃ and Sb₂O₅.

The reference spectrum for Sb₂O₃ contains a well-defined peak at 30500 eV, in agreement with previous work.[37,38] As expected there is a shift to higher energy for Sb₂O₅ − the peak here is found at 30505 eV. The absorption onsets for the doped samples overlap the onset for Sb₂O₃, but the K-edge structure is much broader and the peak maximum is found at even higher energy than for Sb₂O₅ at 30510 eV. This suggest incorporation of the majority of the Sb in the (V) oxidation state, possibly with a minority Sb(III) component. Berry *et al*. have previously demonstrated, using ^{121}Sb Mossbauer spectroscopy, that Sb doping of rutile-TiO₂ results in the bulk substitution of Ti(IV) for Sb(V)[39–41] , in agreement with the results presented here. In a related study Rockenburger *et al.*[42] carried out XANES/EXAFS measurements on Sb:SnO₂ to probe the nature of Sb doping in the bulk of the material. The Sb L_1-edge is sensitive to the oxidation state of Sb. As XANES/EXAFS is atom specific, both the Sb^{3+}/Sb^{5+} show electronic transition from Sb $2s_{1/2}$ levels into partially unoccupied Sb 5p states, the distinction in Sb^{3+}/Sb^{5+} respectively. The results showed that when Sb^{III} precursors were used to prepare samples that there was a strong tendency to form Sb^{V} and more than half the antimony in the samples was oxidised containing Sb in both Sb^{3+}/Sb^{5+}oxidation states. When Sb^{V} was used almost no reduction to Sb^{III} species was observed. They also showed that samples containing both Sb^{3+}/Sb^{5+} had a strong yellowish/brownish colour attributed to intervalence transitions whereas samples with Sb exclusively in the Sb^{V} state remained colourless.

Sb has five valence electrons ($5s^2 5p^3$) so it is reasonable to expect that substitutionally doped Sb(V) would also give rise to additional charge carriers, according to the equation (2):

$$Sb_2O_5 \xrightarrow{2TiO_2} 2Sb_{Ti}^{\cdot} + 4O_O^X + 1/2\, O_{2(g)} + 2e' \tag{2}$$
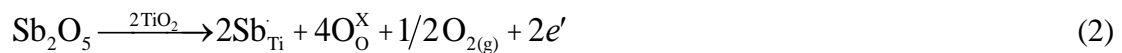
In addition to the scheme shown in (2), competing compensation mechanisms include the formation of Ti vacancies (3) and the formation of interstitial oxygen (4), neither of which will give rise to increased electrical conductivity.

$$2Sb_2O_5 \xrightarrow{5TiO_2} 4Sb_{Ti}^{\cdot} + 10O_O^X + V_{Ti}'''' \tag{3}$$

$$Sb_2O_5 \xrightarrow{2TiO_2} 2Sb_{Ti}^{\bullet} + 4O_O^X + O_i'' \tag{4}$$

Subtracting (2) from (3) gives rise to the reversible redox reaction (5) in which the introduction of *n*-type conductivity requires that the thermodynamic equilibrium of this reaction favours the forward reaction:

$$2O_O^X + V_{Ti}'''' \leftrightarrow O_{2(g)} + 4e' \tag{5}$$

The presence of mobile charge carriers implies that compensation is much less complete than that found for Sb-doped rutile.

3.3 X-ray photoelectron spectroscopy

X-ray photoelectron spectroscopy (XPS) was used to determine the surface atomic concentration of Sb and Ti in the films. The ([Sb]/[Sb]+[Ti])$_{surface}$ ratio, along with the peak positions are shown in Table 1. The O 1s and Sb 3d peaks for 1% and 10% are shown in Fig. 6. The Sb 3d$_{5/2}$ peak overlaps with the O 1s peak, which itself consists of two components. A lower binding energy this is due to lattice oxygen, whereas the higher binding energy peak arises from adventitious surface hydroxide or carbonate. Thus the 3d$_{3/2}$ peak was used to determine the surface Sb concentration and to probe the Sb oxidation state. The curve fit to the overlapping Sb 3d$_{5/2}$ and O 1s peaks assumed a spin orbit splitting of 9.46 eV and that the 5/2 intensity was 1.5 times greater than the 3/2 intensity. Energy-dispersive X-ray spectroscopy (EDX) was used to determine the ratio ([Sb]/[Sb]+[Ti])$_{bulk}$. Both ([Sb]/[Sb]+[Ti])$_{bulk}$ and ([Sb]/[Sb]+[Ti])$_{surface}$ increase with increasing Sb concentration in the solution used for deposition as can be seen in Fig. 7 but the surface Sb concentration is much higher and far exceeds the nominal bulk doping level. At the same time it is apparent that incorporation of Sb into the bulk is not complete at higher nominal doping levels.

The Sb 3d$_{3/2}$ peak occurs around 539.5 eV in all of the films, which is close to literature values for Sb$_2$O$_3$. The corresponding values for Sb$_2$O$_5$ are around 541.0 eV, thus suggesting that the photoelectron spectra from our samples are dominated by Sb(III). The surface Sb to Ti ratios are very much greater than the bulk ratios which suggests that there is a large amount of Sb segregation at the film surface. However as was seen earlier the electrical properties of the films and the X-ray absorption spectra

strongly suggest that Sb is entering the bulk of the material as Sb(V), which in the absence of compensation acts as a one electron donor. In contrast Sb(III) would not give rise to n-type conductivity based on simple electron counting arguments. It is therefore evident that there is a significant amount of Sb(III) surface segregation in the deposited films. Sb(III) surface segregation is well documente in Sb doped SnO$_2$.[43–45] Gulino *et al*[29,32] also demonstrated Sb surface segregation in Sb doped rutile made *via* a co-precipitation method . Using TEM it was shown that at high doping levels (bulk ratios of 4.5% and upwards) an amorphous surface layer a few ionic layers thick was found.[29] Gas phase Sb(III) cations have an electronic configuration of [Kr] 5s^2. In the solid state the internal electronic energy is lowered if Sb(III) occupies non-centrosymmetric sites where mixing between occupied 5s states and nominally empty 5p states is mediated by interaction with O 2p states to give stereochemically active lone pair states.[46,47] Surface sites of necessity lack inversion symmetry, whereas bulk cation sites within the anatase structure are essentially centrosymmetric. This provides a driving force for surface segregation.
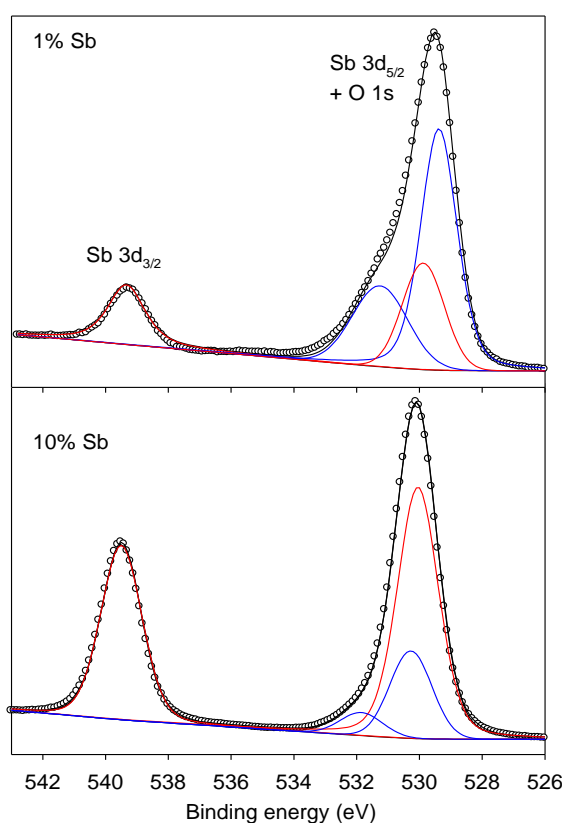

Figure 5: XPS spectra of the O 1s and Sb 3d peaks for (a) 1 mol.% Sb and (b) 10 mol.% Sb doping. The Sb 3d$_{5/2}$ and Sb3d$_{3/2}$ components are shown in red and the O1s components in blue.

Table 2: ([Sb]/[Sb]+[Ti])_bulk and ([Sb]/[Sb]+[Ti])_surface measured using EDX and XPS, respectively, as well as the position of the Sb 3d_{3/2} and Ti 2p_{3/2} peaks.

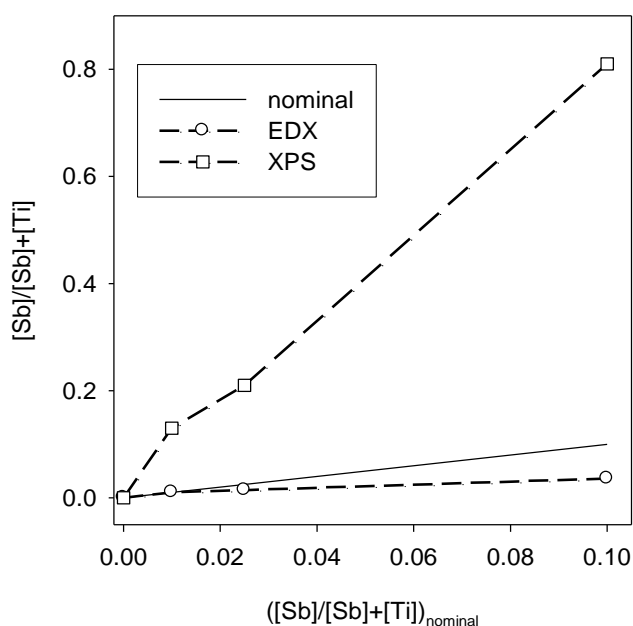| Sample	([Sb]/[Sb]+[Ti])$_{bulk}$	([Sb]/[Sb]+[Ti])$_{surface}$	Sb 3d$_{3/2}$/eV	Ti 3p$_{3/2}$/eV
0 mol.%	0	0	-	459.0
1 mol.%	0.010	0.13	539.4	458.1
2.5 mol.%	0.014	0.21	539.5	458.1
10 mol.%	0.036	0.81	539.5	458.0

Figure 6: The variation in ([Sb]/[Sb]+[Ti])_bulk and ([Sb]/[Sb]+[Ti])_surface with nominal doping level (i.e the Sb concentration in the precursor solution), measured using EDX and XPS respectively. The solid line shows values expected from the nominal doping level.

Valence band XPS are shown in figure 8 for samples with nominal doping levels of 1% Sb, 5% Sb and 10% Sb. The spectrum of the O 2p valence band for the sample with 1% Sb nominal doping level resembles that of undoped anatase and presents two main features: there is a broad peak labelled I at lower binding energy and a somewhat sharper peak labelled II at higher binding energy. In simple terms I corresponds to essentially no bonding O 2p states whereas II derives from bonding states derived from hybridisation between O 2p and Ti 3d or Ti 4s states. A much weaker peak labelled III absent for anatase itself is found on the high binding side of the main valence band. The intensity of peak III increases dramatically with Sb

doping, with indication of a complex lineshape involving two overlapping components. By comparison with photoemission data and DFT calculations for Sn-doped TiO_2 and DFT calculations on Sb oxides, this third peak may be assigned to bonding states derived from covalent mixing between Sb 5s and O 2p states.

In parallel with the growth of peak III, Sb doping leads to growth of intensity above the original O 2p valence band edge. At the lowest (1%) doping level the top off the valence band in the photoemission spectrum is found just over 3 eV below the Fermi energy. This energy corresponds to the bandgap of anatase and implies that the
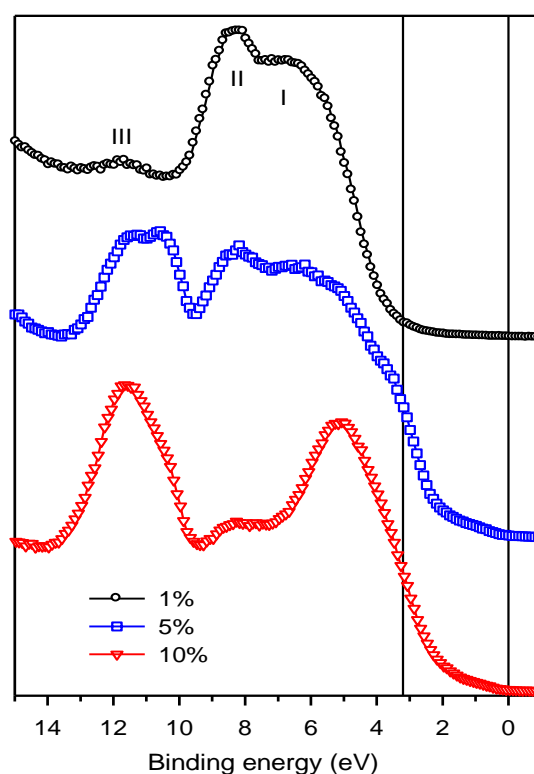

Figure 7: Valence band XPS for thin film samples with nominal doping levels of 1% Sb, 5% Sb and 10% Sb. The solid vertical lines delineate the bandgap of 3.2 eV characteristic of the anatase polymorph of TiO₂.

Fermi energy is pinned close to the minimum of the conduction band, as is to be expected for an n-type material. As the Sb doping level increases spectral intensity increases above the valence band edge, resulting at the highest (nominal 10%) doping level in structure straddling the whole of the bandgap region up to the Fermi energy. This new structure may be assigned to Sb(III) lone pair surface states that arise from an antibonding combination of O 2p and Sb 4s states, that further hybridise with Sb 5p states to give characteristically directional Sb(III) lone pair states. Indeed the XPS

for the 10% Sb doped sample resembles the calculated density of states for Sb_2O_3 where the lone pair character of the uppermost occupied states is revealed by decomposition of the total density of states into its atomic components.[48] Moreover, the fact that occupied states extend all the way to the Fermi energy implies a switchover from n-type to p-type behaviour at the surface. Finally we note that characterisation of filled states extending all the way to the conduction band mimimum explains the pronounced visible region absorption noted earlier. This may now be assigned to transitions from Sb(III) lone pair states associated with segregated Sb at surface and grain boundary interfaces into Ti 3d conduction band states.

Conclusion

Antimony doped TiO_2 (Sb:TiO_2) was deposited on glass substrates *via* aerosol assisted chemical vapour deposition (AACVD) resulting in electrically conductive thin films. The films with the best electrical properties displayed charge carrier concentrations of *ca.* 1×10^{20} cm^{-3} and a specific resistivity as low as 6×10^{-2} Ω.cm essential for emerging titania based TCOs. The incorporation of Sb into the TiO_2 lattice resulted in *n*-type conductivity, leading to a decrease in sheet resistance by four-orders of magnitude compared to that of undoped TiO_2 films. Doping also resulted in orange colouration of the films. Incorporation of Sb into the anatase TiO_2 structure also resulted in a marked difference in the film microstructure compared to undoped TiO_2 potentially useful if nanostructured TiO_2 films are required for a given application.

References

(1)   Fujishima, A. Electrochemical Photolysis of Water at a Semiconductor Electrode. *Nature* **1972**, *238*, 37–38.

(2)   Ni, M.; Leung, M. K. H.; Leung, D. Y. C.; Sumathy, K. A Review and Recent Developments in Photocatalytic Water-Splitting Using TiO2 for Hydrogen Production. *Renew. Sustain. Energy Rev.* **2007**, *11* (3), 401–425.

(3)   Tang, H.; Prasad, K.; Sanjines, R.; Levy, F. TiO2 Anatase Thin Films as Gas Sensors. *Sensors Actuators B Chem.* **1995**, *26* (1–3), 71–75.

(4)   Sunada, K.; Kikuchi, Y.; Hashimoto, K.; Fujishima, A. Bactericidal and Detoxification Effects of TiO2 Thin Film Photocatalysts. *Environ. Sci. Technol.* **1998**, *32* (5), 726–728.

(5)   Palgrave, R. G.; Parkin, I. P. Aerosol Assisted Chemical Vapor Deposition Using Nanoparticle Precursors: A Route to Nanocomposite Thin Films. *J. Am. Chem. Soc.* **2006**, *128* (5), 1587–1597.

(6)   O'regan, B.; Grfitzeli, M. A Low-Cost, High-Efficiency Solar Cell Based on Dye-Sensitized. *Nature* **1991**, *353* (6346), 737–740.

(7)   Morris, D.; Egdell, R. G. Application of V-Doped TiO2 as a Sensor for Detection of SO2. *J. Mater. Chem.* **2001**, *11* (12), 3207–3210.

(8)   Bhachu, D. S.; Sankar, G.; Parkin, I. P. Aerosol Assisted Chemical Vapor Deposition of Transparent Conductive Zinc Oxide Films. *Chem. Mater.* **2012**, *24* (24), 4704–4710.

(9)   Bhachu, D. S.; Waugh, M. R.; Zeissler, K.; Branford, W. R.; Parkin, I. P. Textured Fluorine‐ Doped Tin Dioxide Films Formed by Chemical Vapour Deposition. *Chem. Eur. J.* **2011**, *17* (41), 11613–11621.

(10)   Mo, S.-D.; Ching, W. Y. Electronic and Optical Properties of Three Phases of Titanium Dioxide: Rutile, Anatase, and Brookite. *Phys. Rev. B* **1995**, *51* (19), 13023.

(11)   Labat, F.; Baranek, P.; Domain, C.; Minot, C.; Adamo, C. Density Functional Theory Analysis of the Structural and Electronic Properties of Ti O 2 Rutile and Anatase Polytypes: Performances of Different Exchange-Correlation Functionals. *J. Chem. Phys.* **2007**, *126* (15),

154703.

(12)   Eriksen, S.; Egdell, R. G. Electronic Excitations at Oxygen Deficient TiO2 (110) Surfaces: A

Study by EELS. *Surf. Sci.* **1987**, *180* (1), 263–278.

(13)   Hitosugi, T.; Yamada, N.; Nakao, S.; Hirose, Y.; Hasegawa, T. Properties of TiO2- based

Transparent Conducting Oxides. *Phys. status solidi* **2010**, *207* (7), 1529–1537.

(14)   Egdell, R. G.; Eriksen, S.; Flavell, W. R. Oxygen Deficient SnO 2 (110) and TiO 2 (110): A

Comparative Study by Photoemission. *Solid State Commun.* **1986**, *60* (10), 835–838.

(15)   Dixon, R.; Egdell, R. G.; Beamson, G. Characterisation of Bandgap States in V-Doped TiO2

by High-Resolution X-Ray Photoemission Spectroscopy. *J. Chem. Soc. Faraday Trans.* **1995**,

91 (19), 3495–3497.

(16)   Taverner, A. E.; Rayden, C.; Warren, S.; Gulino, A.; Cox, P. A.; Egdell, R. G. Comparison of

the Energies of Vanadium Donor Levels in Doped SnO 2 and TiO 2. *Phys. Rev. B* **1995**, *51*

(11), 6833.

(17)   Morris, D.; Dixon, R.; Jones, F. H.; Dou, Y.; Egdell, R. G.; Downes, S. W.; Beamson, G.

Nature of Band-Gap States in V-Doped TiO 2 Revealed by Resonant Photoemission. *Phys.

Rev. B* **1997**, *55* (24), 16083.

(18)   Morris, D.; Dou, Y.; Rebane, J.; Mitchell, C. E. J.; Egdell, R. G.; Law, D. S. L.; Vittadini, A.;

Casarin, M. Photoemission and STM Study of the Electronic Structure of Nb-Doped TiO 2.

Phys. Rev. B **2000**, *61* (20), 13445.

(19)   Morgan, B. J.; Scanlon, D. O.; Watson, G. W. Small Polarons in Nb-and Ta-Doped Rutile and

Anatase TiO 2. *J. Mater. Chem.* **2009**, *19* (29), 5175–5178.

(20)   Baumard, J. F.; Tani, E. Electrical Conductivity and Charge Compensation in Nb Doped TiO2

Rutile. *J. Chem. Phys.* **1977**, *67* (3), 857–860.

(21)   Tani, E.; Baumard, J. F. Electrical Properties and Defect Structure of Rutile Slightly Doped

with Cr and Ta. *J. Solid State Chem.* **1980**, *32* (1), 105–113.

(22)   Gao, Y.; Liang, Y.; Chambers, S. A. Synthesis and Characterization of Nb-Doped TiO2 (110)

Surfaces by Molecular Beam Epitaxy. *Surf. Sci.* **1996**, *348* (1–2), 17–27.

(23)   Furubayashi, Y.; Hitosugi, T.; Yamamoto, Y.; Inaba, K.; Kinoda, G.; Hirose, Y.; Shimada, T.;

Hasegawa, T. A Transparent Metal: Nb-Doped Anatase Ti O 2. *Appl. Phys. Lett.* **2005**, *86* (25), 252101.

(24)   Kafizas, A.; Dunnill, C. W.; Parkin, I. P. Combinatorial Atmospheric Pressure Chemical Vapour Deposition (cAPCVD) of Niobium Doped Anatase; Effect of Niobium on the Conductivity and Photocatalytic Activity. *J. Mater. Chem.* **2010**, *20* (38), 8336–8349.

(25)   Furubayashi, Y.; Yamada, N.; Hirose, Y.; Yamamoto, Y.; Otani, M.; Hitosugi, T.; Shimada, T.; Hasegawa, T. Transport Properties of D-Electron-Based Transparent Conducting Oxide: Anatase Ti 1− X Nb X O 2. *J. Appl. Phys.* **2007**, *101* (9), 93705.

(26)   Osorio-Guillén, J.; Lany, S.; Zunger, A. Atomic Control of Conductivity versus Ferromagnetism in Wide-Gap Oxides via Selective Doping: V, Nb, Ta in Anatase TiO 2. *Phys. Rev. Lett.* **2008**, *100* (3), 36601.

(27)   Di Valentin, C.; Pacchioni, G.; Selloni, A. Reduced and N-Type Doped TiO2: Nature of Ti3+ Species. *J. Phys. Chem. C* **2009**, *113* (48), 20543–20552.

(28)   Nogawa, H.; Chikamatsu, A.; Hirose, Y.; Nakao, S.; Kumigashira, H.; Oshima, M.; Hasegawa, T. Carrier Compensation Mechanism in Heavily Nb-Doped Anatase Ti1− xNbxO2+ δ Epitaxial Thin Films. *J. Phys. D. Appl. Phys.* **2011**, *44* (36), 365404.

(29)   Gulino, A.; Taverner, A. E.; Warren, S.; Harris, P.; Egdell, R. G. A Photoemission Study of Sb-Doped TiO2. *Surf. Sci.* **1994**, *315* (3), 351–361.

(30)   Moon, J.; Takagi, H.; Fujishiro, Y.; Awano, M. Preparation and Characterization of the Sb-Doped TiO2 Photocatalysts. *J. Mater. Sci.* **2001**, *36* (4), 949–955.

(31)   Edusi, C.; Sankar, G.; Parkin, I. P. The Effect of Solvent on the Phase of Titanium Dioxide Deposited by Aerosol- assisted CVD. *Chem. Vap. Depos.* **2012**, *18* (4- 6), 126–132.

(32)   Gulino, A.; Condorelli, G. G.; Fragalà, I.; Egdell, R. G. Surface Segregation of Sb in Doped TiO2 Rutile. *Appl. Surf. Sci.* **1995**, *90* (3), 289–295.

(33)   Tang, H.; Levy, F.; Berger, H.; Schmid, P. E. Urbach Tail of Anatase TiO 2. *Phys. Rev. B* **1995**, *52* (11), 7771.

(34)   Burstein, E. Anomalous Optical Absorption Limit in InSb. *Phys. Rev.* **1954**, *93* (3), 632.

(35)   Harunsani, M. H.; Oropeza, F. E.; Palgrave, R. G.; Egdell, R. G. Electronic and Structural

Properties of Sn X Ti1− X O2 (0.0≤ X≤ 0.1) Solid Solutions. *Chem. Mater.* **2010**, *22* (4), 1551–1558.

(36)   Figueiredo, M.; Hedman, B.; Pianetta, P. Extended vs. Local Structure in Sb‐ Pyrochlores: An Illustration of the Valuable Interplay between Crystallography and XAFS. In *AIP Conference Proceedings*; AIP, 2007; Vol. 882, pp 205–207.

(37)   Scheinost, A. C.; Rossberg, A.; Vantelon, D.; Xifra, I.; Kretzschmar, R.; Leuz, A.-K.; Funke, H.; Johnson, C. A. Quantitative Antimony Speciation in Shooting-Range Soils by EXAFS Spectroscopy. *Geochim. Cosmochim. Acta* **2006**, *70* (13), 3299–3312.

(38)   Hockmann, K.; Lenz, M.; Tandy, S.; Nachtegaal, M.; Janousch, M.; Schulin, R. Release of Antimony from Contaminated Soil Induced by Redox Changes. *J. Hazard. Mater.* **2014**, *275*, 215–221.

(39)   Berry, F. J.; Gogarty, P. M. The Oxidation State of Antimony in Antimony-Doped Rutile. *J. Solid State Chem.* **1988**, *73* (2), 588–590.

(40)   Berry, F. J.; Gogarty, P. M.; Jenkins, J. W. An Investigation of the Titanium–antimony–oxygen System by X-Ray Diffraction, Antimony-121 Mössbauer Spectroscopy, and Temperature-Programmed Reduction. *J. Chem. Soc. Dalt. Trans.* **1988**, No. 8, 2161–2166.

(41)   Berry, F. J.; Gogarty, P. M. Antimony-Doped Rutile Titanium (IV) Oxide. *J. Chem. Soc. Dalt. Trans.* **1988**, No. 8, 2167–2170.

(42)   Rockenberger, J.; Zum Felde, U.; Tischer, M.; Tröger, L.; Haase, M.; Weller, H. Near Edge X-Ray Absorption Fine Structure Measurements (XANES) and Extended X-Ray Absorption Fine Structure Measurements (EXAFS) of the Valence State and Coordination of Antimony in Doped Nanocrystalline SnO 2. *J. Chem. Phys.* **2000**, *112* (9), 4296–4304.

(43)   Cox, P. A.; Egdell, R. G.; Harding, C.; Orchard, A. F.; Patterson, W. R.; Tavener, P. J. Free-Electron Behaviour of Carriers in Antimony-Doped Tin (IV) Oxide: A Study by Electron Spectroscopy. *Solid State Commun.* **1982**, *44* (6), 837–839.

(44)   Cox, P. A.; Egdell, R. G.; Harding, C.; Patterson, W. R.; Tavener, P. J. Surface Properties of Antimony Doped Tin (IV) Oxide: A Study by Electron Spectroscopy. *Surf. Sci.* **1982**, *123* (2–3), 179–203.

(45)   Egdell, R. G.; Flavell, W. R.; Tavener, P. Antimony-Doped Tin (IV) Oxide: Surface

Composition and Electronic Structure. *J. Solid State Chem.* **1984**, *51* (3), 345–354.

(46)   Payne, D. J.; Egdell, R. G.; Walsh, A.; Watson, G. W.; Guo, J.; Glans, P.-A.; Learmonth, T.;

Smith, K. E. Electronic Origins of Structural Distortions in Post-Transition Metal Oxides:

Experimental and Theoretical Evidence for a Revision of the Lone Pair Model. *Phys. Rev. Lett.*

2006, *96* (15), 157403.

(47)   Walsh, A.; Payne, D. J.; Egdell, R. G.; Watson, G. W. Stereochemistry of Post-Transition

Metal Oxides: Revision of the Classical Lone Pair Model. *Chem. Soc. Rev.* **2011**, *40* (9), 4455–

4463.

(48)   Allen, J. P.; Carey, J. J.; Walsh, A.; Scanlon, D. O.; Watson, G. W. Electronic Structures of

Antimony Oxides. *J. Phys. Chem. C* **2013**, *117* (28), 14759–14769.